

Assessment of arterially hyper-enhancing liver lesions using virtual monoenergetic images from spectral detector CT: phantom and patient experience

N. Große Hokamp^{1,2,3}, A. J. Höink¹, J. Doerner¹, D. W. Jordan^{2,3}, G. Pahn⁴,
T. Persigehl¹, D. Maintz¹, S. Haneder¹

¹Department of Diagnostic and Interventional Radiology, University Hospital Cologne, Kerpener Str. 62, 50937 Cologne, Germany

²Department of Radiology, University Hospitals Cleveland, Cleveland, OH, USA

³Department of Radiology, School of Medicine, Case Western Reserve University, Cleveland, OH, USA

⁴Philips Clinical Science CT, Hamburg, Germany

Abstract

Purpose To investigate a benefit from virtual monoenergetic reconstructions (VMIs) for assessment of arterially hyper-enhancing liver lesions in phantom and patients and to compare hybrid-iterative and spectral image reconstructions of conventional images (CI-IR and CI-SR).

Methods All imaging was performed on a SDCT (Philips Healthcare, Best, The Netherlands). Images of a non-anthropomorphic phantom with a lesion-mimicking insert (containing iodine in water solution) and arterial-phase images from contrast-enhanced patient examinations were evaluated. VMIs (40–200 keV, 10 keV increment), CI-IR, and CI-SR were reconstructed using different strengths of image denoising. ROIs were placed in lesions, liver/matrix, muscle; signal-to-noise, contrast-to-noise, and lesion-to-liver ratios (SNR, CNR, and LLR) were calculated. Qualitatively, 40, 70, and 110 keV and CI images were assessed by two radiologists on five-point Likert scales regarding overall image quality, lesion assessment, and noise.

Results In phantoms, SNR was increased threefold by VMI_{40keV} compared with CI-IR/SR (5.8 ± 1.1 vs. 18.8 ± 2.2 , $p \leq 0.001$), while no difference was found between CI-IR and CI-SR ($p = 1$). Denoising was

capable of noise reduction by 40%. In total, 20 patients exhibiting 51 liver lesions were assessed. Attenuation was the highest in VMI_{40keV}, while image noise was comparable to CI-IR resulting in a threefold increase of CNR/LLR (CI-IR $1.3 \pm 0.8/4.4 \pm 2.0$, VMI_{40keV}: $3.8 \pm 2.7/14.2 \pm 7.5$, $p \leq 0.001$). Subjective lesion delineation was the best in VMI_{40keV} image ($p \leq 0.01$), which also provided the lowest perceptible noise and the best overall image quality.

Conclusions VMIs improve assessment of arterially hyper-enhancing liver lesions since they increase lesion contrast while maintaining low image noise throughout the entire keV spectrum. These data suggest that to consider VMI screening after arterially hyper-enhancing liver lesions.

Key words: Spectral detector computed tomography—Image quality—Virtual monoenergetic images—Hyper-attenuating liver lesions

Abbreviations

VMI	Virtual monoenergetic image
DECT	Dual-energy computed tomography
DSCT	Dual-source computed tomography
SDCT	Spectral detector computed tomography
CI-IR	Conventional images reconstructed with an hybrid-iterative reconstruction algorithm
CI-SR	Conventional images reconstructed with the spectral reconstruction algorithm
LLR	Lesion-to-liver ratio

Electronic supplementary material The online version of this article (<https://doi.org/10.1007/s00261-017-1411-1>) contains supplementary material, which is available to authorized users.

Correspondence to: N. Große Hokamp; email: nils.grosse-hokamp@uk-koeln.de

Computed tomography (CT) is one of the key tools for detection and characterization of focal liver lesions. Primary hepatic lesions, such as hemangiomas or hepatocellular carcinoma, and secondary hepatic lesions like metastases from melanoma, renal cell carcinoma, neuroendocrine tumors, thyroid cancer, breast cancer, and sarcoma are hyper-attenuating in CT images [1, 2]. In contrast-enhanced CT, hyper-attenuation is typically caused by an increased uptake of Iodinated contrast agent in the selected contrast phase, resulting from hyper-vascularization of the lesion compared with liver parenchyma [3–5].

In CT, attenuation of X-rays is caused by the photoelectric effect (which is predominant for photon energies below 100 keV) and the Compton effect (which gains importance for photon energies above 100 keV) [6, 7]. For several years, dual-energy CT (DECT) scanners that assess these effects separately have been available [8]. DECT allows reconstruction of virtual monoenergetic images (VMIs) which approximate the result of an acquisition with a true monoenergetic X-ray beam; these are typically available in a range from 40 to 200 keV [9, 10]. Since the photoelectric effect is greatly influenced by the atomic number ($\sim Z^4$), VMI of lower energies (VMI_{low}) improve soft tissue contrast and improve visualization of Iodine-based contrast media ($Z = 53$) compared with human tissue ($Z_{average} < 15$), particularly for photon energies in the proximity of the k-edge energy of iodine (≈ 33 keV) [7, 9, 10].

It has been shown that VMI_{low} facilitate and improve the assessment of arterially hyper-enhancing liver lesions in dual-source DECT [11, 12]. Further, the feasibility of DECT to allow for material decomposition and for quantification of contrast media (as a surrogate parameter for lesion vascularization) on contrast-enhanced DECT has been demonstrated [6, 13].

For several years, emission-based DECT scanner designs have been available, using two X-ray spectra of different mean energies which are generated either (a) in two separate scans at different tube voltages (sequential scanning), (b) by repeated switching of the tube voltage within a single rotation (kV-switching), or (c) in two separate tube-detector systems within one scanner (dual-source CT, DSCT) [6]. Recently, the first detector-based approach, referred to as spectral detector computed tomography (SDCT), was introduced [14, 15]. The detector consists of two layers, an upper yttrium-based layer detecting the low-energy incident photons, and a gadolinium oxysulfide-based lower layer in which photons of higher energy are detected. The design enables acquisition of fully temporally and spatially matched dual-energy projection data within an unrestricted field of view [14]. Information from both detector layers can be combined for reconstruction of conventional CT images using hybrid-iterative reconstruction algorithms (CI-IR) that have been investigated earlier [16–18]. For

dual-energy results, a dedicated spectral reconstruction algorithm is provided that allows for reconstruction of VMIs and conventional images (CI-SR). While CI-IR and CI-SR seem visually similar, neither has this been disclosed by the vendor explicitly nor is any literature is available on this.

The aim of this study was to investigate quantitative and qualitative image qualities of conventional and virtual monoenergetic images from SDCT for assessment of arterially hyper-enhancing focal liver lesions in phantoms and in vivo. The phantom portion focuses on different iterative and spectral reconstruction algorithms especially in terms of noise, and the patient portion focuses on signal-to-noise and contrast-to-noise ratios as well as subjective measures of image quality.

Materials and methods

Phantom design

A standardized, non-anthropomorphic phantom for quality control with inserts of different densities was used in this study (Gammex 464 with Body Ring, Sun Nuclear Corporation, Middleton, WI, USA). Overall, the phantom has an oval shape to mimic attenuation by a human body with a dimension of 26.4×33.0 cm. Its matrix material exhibits water-equivalent HU values. We planned to mimic arterially hyper-enhancing liver lesions by inserting an acrylic tube (diameter 26 mm) containing a solution of iodinated contrast agent in water (Accupaque 350 mg/mL, GE Healthcare; Little Chalfort, UK). To determine an appropriate concentration of contrast agent, preliminary experiments with different concentrations were conducted (data not shown). Here, a concentration of 0.75 mg/cm³ was found to best represent mean attenuation of patient's lesions (determined as described below).

Study population and lesion selection

The institutional review board approved this technical feasibility study and waived informed consent due to the retrospective study design. A structured search was carried out within the radiology information system with the following inclusion criteria: (a) age > 18 years, (b) bi-phasic SDCT between June and July 2017, (c) examination with a standardized imaging protocol as described below, (d) known cancer with potential hyper-vascularized liver metastasis (melanoma, breast cancer, sarcoma, or neuroendocrine tumors), and (e) report of a hyper-attenuating liver lesion. Exclusion criteria comprised (a) age ≤ 18 years, and (b) modified imaging protocol and incomplete image reconstructions. In total, 28 patients were identified exhibiting a total of 69 arterially hyper-enhancing focal liver lesions. Two board-certified radiologists (AJH, SH) with 8 and 9 years of experience, respectively, in abdominal CT determined the nature of the liver lesions in consensus considering all available

information including clinical information, histology, follow-up CT (minimum time between CT: 6 months), magnetic resonance imaging, and/or (contrast-enhanced) ultrasound. Arterially hyper-enhancing liver metastases ($n = 16$) and hemangiomas ($n = 35$) were included, while lesions indeterminable upon available information ($n = 18$) were excluded from further assessment. Hence, the final analysis included 51 lesions of 7.2 ± 5.1 mm along axis diameter in 20 patients (9 males, 11 females; mean age 62 ± 15 years, range 39–83 years).

Image acquisition

All scans were performed on a clinical SDCT scanner (IQon, Philips Healthcare, Best, The Netherlands). Patients were imaged in head-first supine position. A body weight-adapted volume of non-ionic, iodinated contrast agent (Accupaque 350 mg/mL, GE Healthcare; Little Chalfort, UK) was administered intravenously via a peripheral vein with a mean flow of 3.5 mL/s followed by a 30 mL saline flush. The scans were started with delays of 16 and 50 s after reaching the threshold value of 150 HU in the abdominal aorta for the arterial and venous phases, respectively. Tube current modulation was activated in all patients (DoseRight 3D-DOM; Philips Healthcare, Best, The Netherlands). Phantom scans used fixed tube current of 100 mAs and were repeated five times. Additional scan parameters used in both patient and phantom scans were collimation 64×0.625 mm; rotation time 0.5 s; pitch 0.671; tube voltage 120 kVp.

Image reconstruction

Image reconstruction for further analysis was limited to the arterial phase only. All images were reconstructed in the transaxial plane with slice thickness 2 mm and section increment 1 mm.

Phantom

Conventional images were reconstructed using a hybrid-iterative image reconstruction algorithm (CI-IR, iDose⁴, Philips Healthcare, Best, The Netherlands) with a standard soft tissue kernel (B) and with presets for none, medium, and high denoising (0, 3, and 6, respectively). To obtain spectral results, image reconstruction with a dedicated spectral reconstruction algorithm is required (Spectral B, Philips Healthcare, Best, The Netherlands). This spectral algorithm was applied to obtain VMI of each 10 keV increment in the range 40–200 keV and conventional images (CI-SR). Again, presets for none, medium, and high denoising were chosen (0, 3, and 6, respectively).

Patients

In patients, image reconstruction of arterial phase was limited to a medium denoising level (3) and to CI-IR and

VMI images of 40–200 keV with a 10 keV increment using the above-named reconstruction algorithms and kernel.

Quantitative assessment

Image analysis was performed on a standard DICOM image viewer (Osirix v8.0, Pixmeo, Bernex, Switzerland).

Phantom

Circular regions of interest (ROI) of 1.0 cm^2 area were drawn in five consecutive slices in the matrix material and the customized insert in CI-IR images. ROIs were then copied and pasted to CI-SR and VMI datasets. ROI attenuation mean and standard deviation (SD) in Hounsfield Units (HU) were recorded, and the measurements of repeated scans were averaged. Signal-to-noise ratio was calculated as $\text{SNR} = \text{HU}_{\text{insert}} / \text{SD}_{\text{matrix}}$ adapted from previous studies [19, 20].

Patients

Circular ROIs were placed in the following structures in arterial phase: lesions ($1 \times$), liver parenchyma ($3 \times$), psoas muscle ($2 \times$), subcutaneous fat ($2 \times$), and abdominal aorta ($2 \times$). All ROI were drawn as large as possible (at least 0.5 cm^2) excluding unrepresentative structures such as vessels, fasciae, and bile ducts. ROIs were placed in CI-IR images and copied and pasted to matching locations in VMIs. Mean and standard deviation (SD) of attenuation in Hounsfield Units (HUs) were recorded and averaged where applicable. Image noise was represented by standard deviation in psoas muscle. Signal-to-noise ratio of a ROI_x was defined as $\text{SNR}_x = \text{HU}_x / \text{SD}_x$; Contrast-to-noise ratio of a ROI_x as $\text{CNR}_x = |\text{HU}_x - \text{HU}_{\text{muscle}}| / \text{SD}_{\text{muscle}}$; and lesion-to-liver ratio as $\text{LLR} = |\text{HU}_{\text{lesion}} - \text{HU}_{\text{liver}}| / \text{SD}_{\text{liver}}$, being adapted from previous studies [11, 21–24].

Qualitative assessment

To assess relevant changes in subjective image quality in patient examinations, evaluation was limited to CI-IR and three representative VMI energy levels (40, 70, and 110 keV). The same two radiologists who initially characterized the lesions 6 weeks later determined the subjective image quality, blinded to the reconstruction technique and patient history. Rating was performed in consensus with regard to overall image quality, image noise, and delineation of hepatic lesions on five-point Likert scales: for overall image quality, ranging from 1 = severely impaired image quality/non-diagnostic to 5 = excellent image quality/high diagnostic certainty; for image noise, ranging from 1 = excessive noise to 5 = images without noticeable noise; and for delineation and contrast of the lesion, ranging from 1 = lack of

delineation and poor, non-diagnostic lesion contrast to 5 = perfect delineation of the lesion with excellent, strong lesion contrast. Next, the conventional reconstruction (CI-IR) was identified, and the same radiologists were asked to rank VMI reconstructions compared with CI-IR as a reference. The imaging features, as described above (image quality, image noise, delineation of hepatic lesions), were ranked as + 2 (much better)/+ 1 (better)/0 (equal)/- 1 (worse)/- 2 (much worse) compared with CI-IR). Readers were explicitly free to adjust window settings.

Statistical analysis

Interval scaled data are reported as mean \pm standard deviation, ordinal scaled data as median and quartile-range. Descriptive statistics are given as fractions. Statistical analysis was performed using GraphPad Prism (GraphPad Software, Version 6, La Jolla, CA, USA) applying ANOVA with Bonferroni's post hoc (for interval scaled), Kruskal-Wallis and Wilcoxon signed-rank test (for ordinal scaled data). Statistical significance was defined as $p \leq 0.05$.

Results

Phantom measurements

Mean attenuation of the insert in conventional image reconstructions was comparable to the patients' lesions (phantom 132.2 HU vs. patients 135.6 HU). No difference between CI-IR and CI-SR was observed, therefore the further analysis in patients was limited to CI-IR (Table 1, Fig. 1). As expected, attenuation was the highest in 40 keV images and decreased at higher keV levels; the different denoising levels did not alter attenuation ($p \leq 0.05$). Image examples can be found in Online Resources 1 and 2.

No difference in image noise between CI-IR and CI-SR was observed. 40 keV VMI exhibited the highest image noise, while image noise decreased at higher keV levels ($p \leq 0.05$, Table 1, Fig. 1). Noise at denoising level 6 (strongest) was 32%–42% lower for the matrix material and 42%–46% lower for the insert compared with non-denoised images (level 0) for corresponding reconstructions ($p \leq 0.05$). The highest SNR values were found at 40 keV with the strongest (level 6) denoising levels employed.

Patients: qualitative assessment

Attenuation

Lesions exhibited average attenuation of 135.6 ± 40.2 HU in CI-IR. For VMIs, a stepwise decrease in the absolute attenuation values of the lesions was found from low to high keV. Compared with CI-IR, lesions exhibited higher attenuation in VMI_{low} images (40 and 50 keV) and lower attenuation values in high keV (90–200 keV) reconstructions (Fig. 2A, Table 2). The liver parenchyma exhibited the highest attenuation in 40 keV images (CI-IR vs. 40 keV/200 keV: 74.4 ± 13.4 HU vs. 116.0 ± 38.9 HU, $p \leq 0.001/59.8 \pm 6.3$ HU, n.s.). Further attenuation values are listed in Table 2.

Noise

Image noise was significantly lower in any VMI reconstruction compared with CI-IR ($p \leq 0.05$, Table 2, Fig. 2B). In VMIs, noise decreased slightly for VMI images from 40 to 60 keV, followed by a relatively constant noise level up to 200 keV.

Signal-to-noise ratio (SNR)

VMI_{low} images had higher SNR in patients. SNR for lesions was significantly higher for 40 and 50 keV VMIs

Table 1. Quantitative image parameters for phantom measurements

		Denoising level	CI-IR	CI-SR	40 keV	70 keV	110 keV	200 keV
Attenuation	Matrix	0	0.9 ± 1.3	0.9 ± 1.3	4.0 ± 1.6	1.9 ± 0.7	1.2 ± 0.8	1.0 ± 1.0
		3	1.0 ± 1.1	1.0 ± 1.1	3.9 ± 1.2	1.9 ± 0.6	1.3 ± 0.7	1.1 ± 0.9
		6	1.0 ± 1.0	1.0 ± 1.0	3.9 ± 1.2	1.9 ± 0.5	1.3 ± 0.7	1.2 ± 0.8
	Insert	0	132.3 ± 14.4	132.3 ± 14.4	375.0 ± 100.2	149.6 ± 20.5	78.8 ± 9.1	53.7 ± 16.9
		3	132.3 ± 13.9	132.3 ± 13.9	376.5 ± 99.3	149.7 ± 20.2	78.4 ± 9.0	53.2 ± 16.6
		6	132.3 ± 13.5	132.3 ± 13.5	376.7 ± 98.0	149.7 ± 20.2	78.3 ± 8.6	53.1 ± 16.0
Noise	Matrix	0	22.7 ± 1.7	22.7 ± 1.7	20.0 ± 1.9	18.7 ± 1.4	18.4 ± 1.3	18.3 ± 1.2
		3	17.7 ± 1.4	17.7 ± 1.4	15.4 ± 1.6	14.4 ± 1.1	14.1 ± 1.0	14.1 ± 0.9
		6	12.7 ± 1.1	12.7 ± 1.1	11.0 ± 1.4	10.0 ± 0.9	9.7 ± 0.7	9.7 ± 0.7
	Insert	0	24.6 ± 2.8	24.6 ± 2.8	44.6 ± 11.4	22.1 ± 2.7	18.8 ± 1.0	18.5 ± 0.6
		3	20 ± 2.7	20 ± 2.7	42.3 ± 11.1	18.3 ± 3.0	14.6 ± 0.8	14.6 ± 0.5
		6	15.6 ± 2.7	15.6 ± 2.7	39.1 ± 11.5	14.8 ± 3.3	10.8 ± 0.8	10.9 ± 0.5
SNR	SNR	0	5.8 ± 1.1	5.8 ± 1.1	18.8 ± 2.2	8.0 ± 1.2	4.3 ± 1.0	2.9 ± 1.0
		3	7.5 ± 1.1	7.5 ± 1.1	24.5 ± 2.8	10.4 ± 1.3	5.6 ± 1.0	3.8 ± 1.0
		6	10.4 ± 1.2	10.4 ± 1.2	34.1 ± 3.5	14.9 ± 1.5	8.1 ± 1.1	5.5 ± 1.1

Attenuation, standard deviation (SD) and Signal-to-noise ratio (SNR) for an insert containing a solution of an iodinated contrast agent ($c = 0.75$ mg/cm³) using hybrid-iterative and spectral reconstruction algorithm for conventional images (CI-IR and CI-SR, respectively) and SR for different VMI levels (40, 70, 110 and 200 keV) with different presets for none, medium and high denoising applied (0, 3 and 6, respectively)

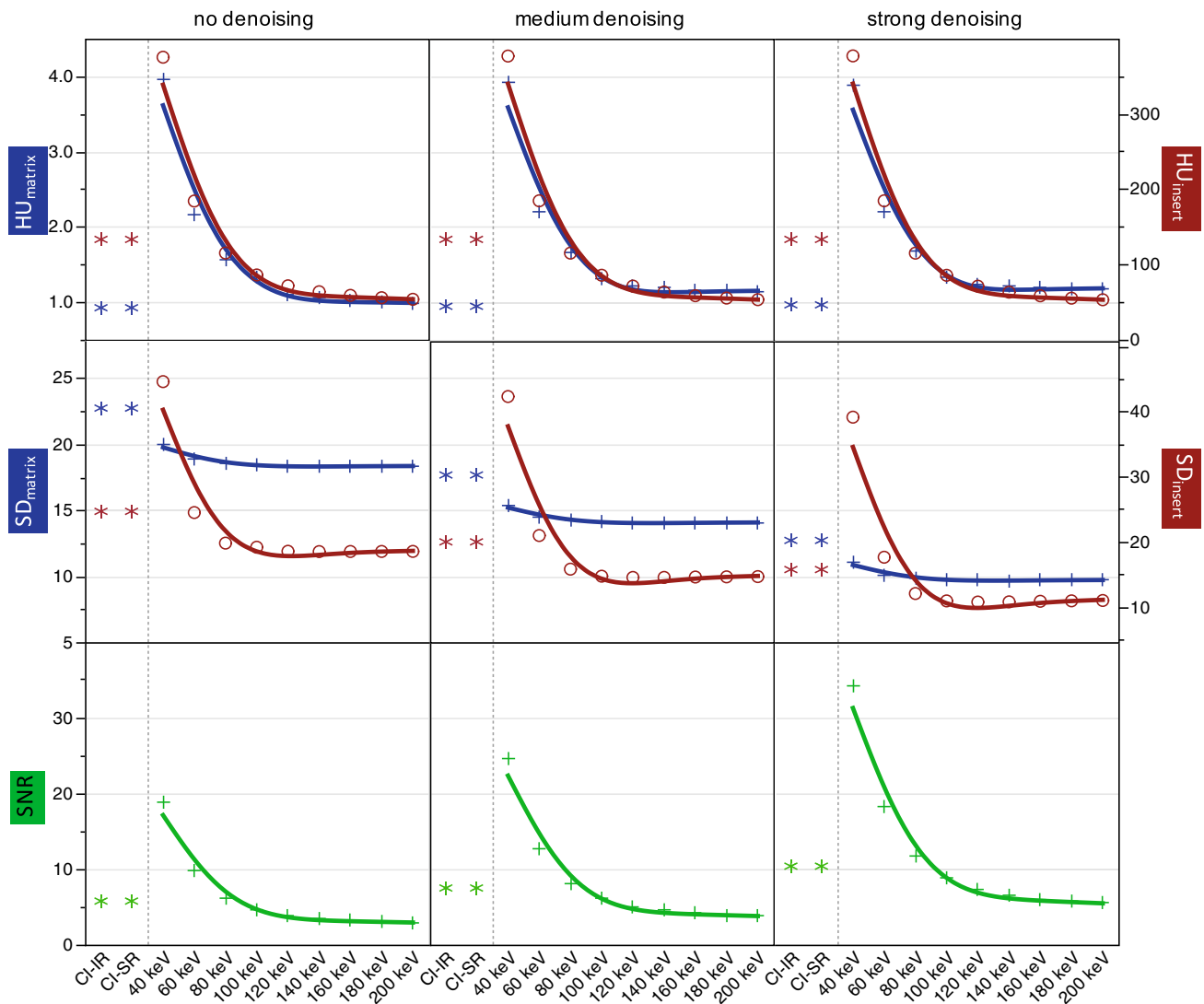


Fig. 1. Attenuation (HU), noise (SD) and signal-to-noise ratio (SNR) for matrix material (blue, +) of the phantom and the insert (red, o) with an iodine-based solution for different reconstructions and presets for image denoising. Attenuation did neither change between iterative and spectral reconstruction of conventional images (CI-IR and CI-SR), nor any

denoising preset, while noise did decrease with increase of denoising strength. Remarkably, the iodine-based insert led to a clear increase of both, attenuation and noise in the proximity of the k-edge of iodine. SNR was the highest in low-keV virtual monoenergetic images and increased with the denoising strength.

($p \leq 0.01$; Table 2). For liver parenchyma, SNR was higher for 40–70 keV VMIs compared with CI-IR (Table 2).

Contrast-to-noise ratio (CNR)

CNR of lesions was the highest in 40 keV VMI and decreased with the increasing VMI keV levels ($p \leq 0.05$). Statistically significant differences from CI-IR were observed for 40–60 keV VMIs (Table 2).

Lesion-to-liver ratio (LLR)

The contrast between liver parenchyma and lesions was significantly higher in VMI images from 40 to 60 keV

compared with conventional reconstructions and lower in images of 100 keV and above ($p \leq 0.05$; Table 2, Fig. 2C).

Subjective image quality

Overall image quality was comparable in CI-IR; 40 and 70 keV VMI images with a slight tendency toward improved image quality in 40 keV images ($p > 0.05$). 110 keV VMI images were rated significantly inferior to both 40 keV VMI image and CI-IR (CI-IR/40 vs. 110 keV: 4 (2–5)/4 (3–5) vs. 3 (2–4), $p \leq 0.001$, Fig. 3A). Regarding subjective image noise, 40 keV images were rated the best, while 110 keV VMI images received the

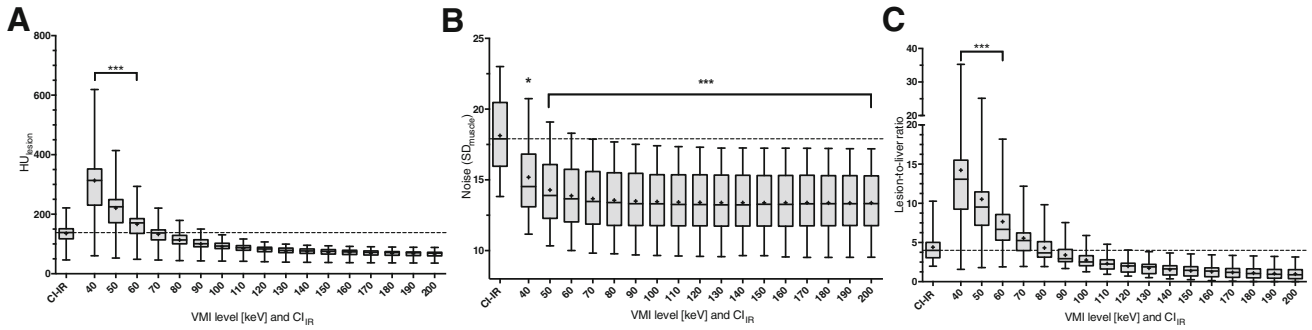


Fig. 2. Illustration of the image mean attenuation of the liver lesions (HU) clearly reveals higher attenuation in low-keV virtual monoenergetic images compared with conventional images (A). Noise, as depicted by standard deviation (SD) of the psoas muscle, differed in dependency of keV level in virtual monoenergetic reconstructions (VMIs); however, it was found to be lower in any VMI compared with CI-IR (B). This

resulted in clear superiority of the lesion-to-liver ratio in 40–60 keV images compared with CI-IR (C). Significant differences compared with CI are indicated ($*p \leq 0.05$; $***p \leq 0.001$); geometric (–) and arithmetic mean (+) are indicated within the boxplots; the mean for conventional images (CI-IR) is indicated throughout the other boxplots (horizontal, dotted line).

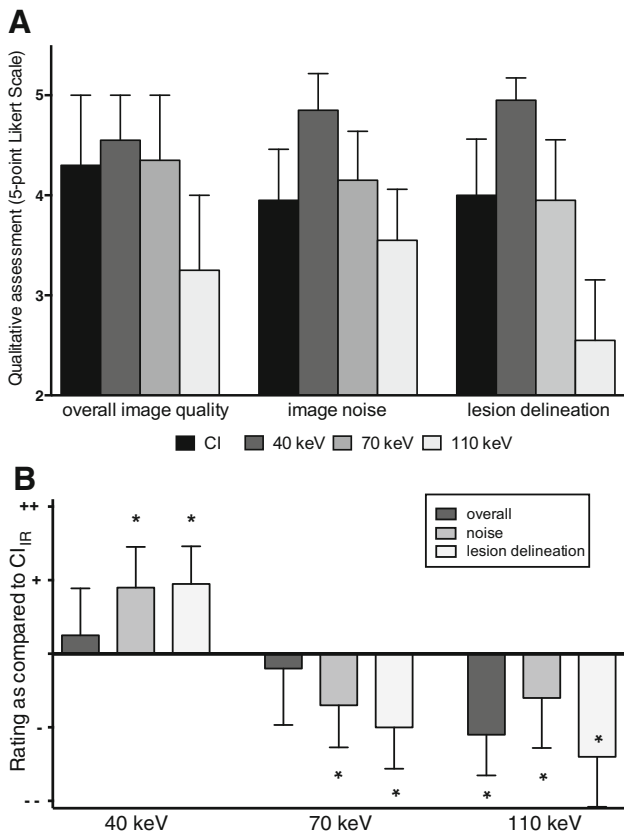


Fig. 3. Rating for conventional (CI), and virtual monoenergetic images (VMIs) of 40, 70, and 110 keV regarding overall image quality, images’ noise, and lesion delineation on five-point Likert-scales (A). Subjective ranking of the above-named VMI images compared with CI-IR illustrates superiority and inferiority of 40 keV and 110 keV images, respectively. (B). Significant differences compared with CI-IR are indicated (*).

lowest ratings (5 (4–5) and 3 (3–4), respectively, $p \leq 0.001$). Lesion delineation in 40 keV images was rated superior to the other reconstructions, while CI-IR and 70 keV VMI image showed comparable ratings (CI-IR vs. 40/70 keV: 4 (3–5) vs. 5 (4–5), $p \approx 1$, Figs. 3A, 4).

In ranking compared with CI-IR, 40 keV images exhibited comparable overall image quality ($p = 0.18$), while image noise and lesion delineation were ranked superior to CI-IR (both $p \leq 0.01$, Fig. 3B). 110 keV images were ranked significantly inferior to CI-IR in all three categories ($p \leq 0.05$).

Discussion

This study aimed to investigate quantitative and qualitative imaging parameters from conventional and VMI reconstructions for the assessment of arterially hyper-enhancing focal liver lesions.

The phantom portion focused on quantitative imaging parameters. Together with SDCT a corresponding spectral reconstruction algorithm was introduced. We found that conventional images reconstructed with this algorithm are identical in terms of attenuation and noise to images reconstructed with the vendor’s hybrid-iterative reconstruction algorithm (IR), which has been extensively examined on multidetector CT [25, 26]. As expected, mean attenuation was unaffected by the different levels of image denoising in CI, while noise did decrease around 40% at the strongest denoising level. According to the vendor, the lowest setting for denoising in the IR algorithm is equivalent to filtered back projection; however, in SDCT, a minimal degree of denoising is performed to combine the two detector layers.

The highest attenuation by the iodine insert was found in 40 keV VMI, as expected due to the proximity of this energy to the iodine k-edge [9, 11, 27]. Accord-

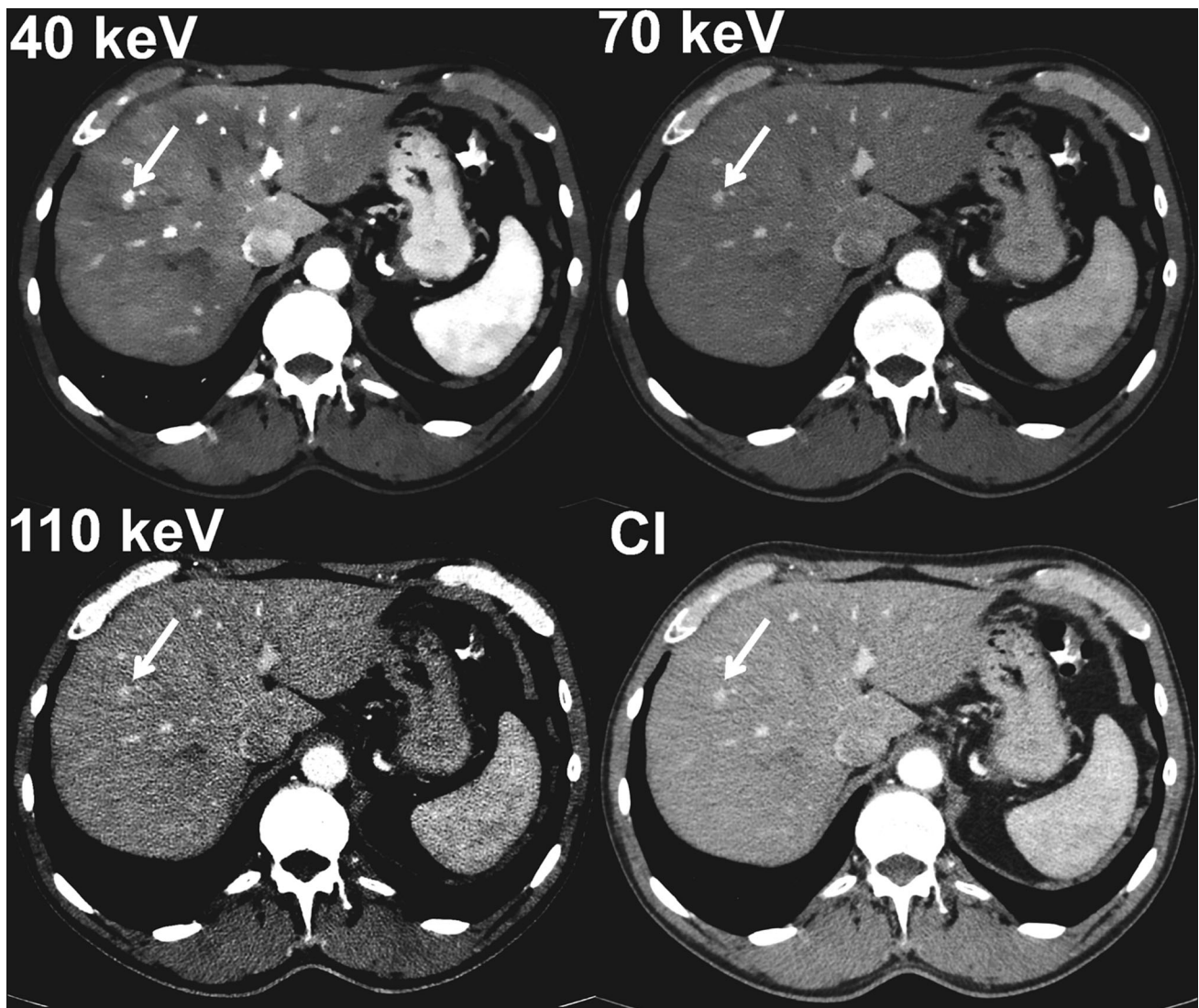


Fig. 4. Axial CT-image of a 55-year-old male with history of melanoma exhibiting a hemangioma in segment VIII. The hemangioma is visible in the conventional image (CI) as well as for VMI images of 40, 70, and 110 keV. However, as

suggested by the lesion-to-liver ratio, the hemangioma stands out much clearer in 40 keV images compared with 70 keV images and CI. Window levels were adjusted for each reconstruction.

ingly, noise was the highest in 40 keV images as well. Remarkably, noise in the matrix material remained approximately constant across the entire range of keV choices. The increased attenuation outweighed the increase in noise at low keV, such that 40 keV images yielded a threefold higher SNR compared with CI-IR/SR.

The findings from the phantom experiments were confirmed in vivo: low-keV VMI reconstructions yielded higher attenuation for both liver parenchyma and hepatic lesions. The noise level remained low as expected from the phantom measurements resulting in increases in CNR and SNR values across the entire keV range, e.g., in 40 keV reconstructions with a threefold higher lesion-to-liver ratio compared with CI.

Therefore, the two key technical findings are: (a) attenuation boost in low-keV VMI in combination with (b) low image noise throughout the entire range of available VMI reconstructions. The first aspect is well known from multiple previous DECT studies; however, in those studies, the use of low-keV VMI (< 60 keV) was typically limited due to drastically increased image noise [11, 28, 29]. Reduced image noise is a novel aspect in SDCT and can most likely be explained by the detector-based dual-energy approach. The two stacked detector layers of SDCT allow for temporally and spatially matched acquisition of low and high energy datasets, which enables exploitation of the anti-correlation of noise between the two DECT base datasets for overall noise suppression [30, 31]. Further reduction of image

Table 2. Quantitative image parameters for patient measurements

	CI-IR	40 keV	70 keV	110 keV	200 keV
Noise (SD_{muscle})	18.1 ± 2.6	15.2 ± 2.7	13.7 ± 2.3	13.4 ± 2.2	13.4 ± 2.2
Lesion					
Attenuation	135.6 ± 40.2	313.4 ± 125.9	132.8 ± 36.6	84.8 ± 17.6	66.4 ± 11.7
SNR	9.7 ± 5.4	17.4 ± 13.9	11.3 ± 6.6	9.1 ± 5.4	7.6 ± 4.5
CNR	5.0 ± 2.6	17.8 ± 9.7	6.3 ± 3.2	2.9 ± 1.6	1.5 ± 1.0
Liver					
Attenuation	74.4 ± 13.4	115.9 ± 38.9	75.2 ± 13.4	66.0 ± 7.6	59.8 ± 6.3
SNR	4.9 ± 1.0	7.9 ± 2.9	6.6 ± 1.5	5.9 ± 1.0	5.5 ± 0.9
CNR	1.3 ± 0.8	3.8 ± 2.7	1.8 ± 1.0	1.2 ± 0.6	0.9 ± 0.5
Lesion-to-liver ratio	4.4 ± 2.0	14.2 ± 7.5	5.5 ± 2.2	2.3 ± 0.9	1.0 ± 0.7

Attenuation, image noise, Signal-to-noise ratio (SNR), and Contrast-to-noise ratio (CNR) for arterially hyper-enhancing liver lesions and liver parenchyma in different VMI levels and in conventional images (CI). In addition, the lesion-to-liver ratio is indicated for the same reconstructions

noise is achieved by the use of iterative methods in the dedicated spectral reconstruction algorithm [32–34]. Among other DECT implementations, only the kVp-switching technique enables VMI reconstruction within the projection domain; however, because raw data are acquired neither in temporal nor spatial coherence, interpolation is necessary for post-processing in the projection domain [6, 35]. Generally, methods for VMI reconstruction in the image domain result in increased image noise [30]; however, this problem is addressed by a new reconstruction algorithm available for third-generation DSCT that the characteristic peak of SNR- and CNR at 70 keV towards lower energies, resulting in continuous increase of SNR and CNR with lower energies analogous to SDCT [28, 33].

Subjective image evaluation by experienced radiologists agreed with quantitative findings in terms of image noise. Overall image quality was rated superior or equal to CI in 40 and 70 keV images, respectively. Lesion delineation on 40 keV images was significantly better compared with CI which is a direct effect of increased contrast between lesion and liver parenchyma; however, further work is needed to determine if these reconstructions can be used for robust lesion size assessment due to possible blooming contrast.

There are several limitations to this study. First, this study was designed to assess known lesions (only hemangiomas and metastasis, excluding other types such as hepatocellular carcinomas) and to investigate their imaging properties in terms of objective and subjective image qualities. Thus, diagnostic certainty or accuracy were not investigated. To the authors' knowledge, no previous study has provided phantom and clinical data on VMI reconstructions from SDCT with a focus on arterially hyper-enhancing liver lesions. Regarding phantom measurements, it needs to be mentioned that although the inserts did mimic imaging properties of arterially hyper-enhancing lesions, the matrix material showed water-equivalent attenuation values. This might result in an overestimation of the SNR. Having demonstrated the feasibility of improved image quality in this study, the diagnostic impact of this technique needs

to be addressed in future studies. Second, we assessed image noise by measurement of standard deviation in an ROI, which is not physically correct in images derived from iterative reconstruction.

Conclusion

SDCT allows for reconstruction of conventional CT images that are identical with established hybrid-iterative image reconstruction. Further, it allows reconstruction of virtual monoenergetic images that provide a relatively low noise level throughout the entire keV spectrum and yield increases of signal-to-noise and contrast-to-noise ratios in arterially hyper-enhancing liver lesions. Accordingly, subjective lesion visualization and delineation is improved. We suggest using low-energy (~ 40 keV) VMI from SDCT when examining the liver for arterially hyper-enhancing lesions, particularly in patients with tumors known for hyper-vascularized metastases.

Compliance with ethical standards

Funding No funding were received for this study.

Conflict of interest GP is an employee of Philips Healthcare. DM received reimbursements for talks outside this specific project from Philips Healthcare. NGH, AJH, JD, DWJ, TP, and SH all declare that they have no conflict of interest.

Ethical approval All procedures performed in studies involving human participants were in accordance with the ethical standards of the institutional and/or national research committee and with the 1964 Helsinki declaration and its later amendments or comparable ethical standards.

Informed consent The institutional review board approved this study and waived informed consent due to the retrospective study design.

Human and animal rights This article does not contain any studies with animals performed by any of the authors.

References

1. Kanematsu M, Kondo H, Goshima S, et al. (2006) Imaging liver metastases: review and update. *Eur J Radiol* 58:217–228. <https://doi.org/10.1016/j.ejrad.2005.11.041>
2. Bressler EL, Alpern MB, Glazer GM, Francis IR, Ensminger WD (1987) Hypervascular hepatic metastases: CT evaluation. *Radiology* 162:49–51. <https://doi.org/10.1148/radiology.162.1.3024210>

3. Burkholz KJ, Silva AC (2008) AJR teaching file: hypervascular metastasis or hepatic hemangioma? *Am J Roentgenol* 190:53–56. <https://doi.org/10.2214/AJR.07.7074>
4. Klotz T, Montoriol PF, Da Ines D, et al. (2013) Hepatic haemangioma: common and uncommon imaging features. *Diagn Interv Imaging* 94:849–859. <https://doi.org/10.1016/j.diii.2013.04.008>
5. Burgener FA, Hamlin DJ (1983) Contrast enhancement of focal hepatic lesions in CT: effect of size and histology. *Am J Roentgenol* 140:297–301. <https://doi.org/10.2214/ajr.140.2.297>
6. McCollough CH, Leng S, Yu L, Fletcher JG (2015) Dual- and multi-energy CT: principles, technical approaches, and clinical applications. *Radiology* 276:637–653. <https://doi.org/10.1148/radiol.2015142631>
7. Bushberg JT (1998) The AAPM/RSNA physics tutorial for residents. X-ray interactions. *Radiographics* 18:457–468. <https://doi.org/10.1148/radiographics.18.2.9536489>
8. Flohr TG, McCollough CH, Bruder H, et al. (2006) First performance evaluation of a dual-source CT (DSCT) system. *Eur Radiol* 16:256–268. <https://doi.org/10.1007/s00330-005-2919-2>
9. Riederer SJ, Mistretta CA (1977) Selective iodine imaging using K-edge energies in computerized X-ray tomography. *Med Phys* 4:474–481. <https://doi.org/10.1118/1.594357>
10. Manjunatha HC, Rudraswamy B (2013) Study of effective atomic number and electron density for tissues from human organs in the energy range of 1 keV–100 GeV. *Health Phys* 104:158–162. <https://doi.org/10.1097/HP.0b013e31827132e3>
11. Shuman WP, Green DE, Busey JM, et al. (2014) Dual-energy liver CT: effect of monochromatic imaging on lesion detection, conspicuity, and contrast-to-noise ratio of hypervascular lesions on late arterial phase. *Am J Roentgenol* 203:601–606. <https://doi.org/10.2214/AJR.13.11337>
12. Yeh BM, Shepherd JA, Wang ZJ, et al. (2009) Dual-energy and low-kVp CT in the abdomen. *AJR Am J Roentgenol* 193:47–54. <https://doi.org/10.2214/AJR.09.2592>
13. Thieme SF, Johnson TRC, Lee C, et al. (2009) Dual-energy CT for the assessment of contrast material distribution in the pulmonary parenchyma. *Am J Roentgenol* 193:144–149. <https://doi.org/10.2214/AJR.08.1653>
14. De Cecco CN, Laghi A, Schoepf UJ, Meinel FG (2015) Dual Energy CT. *Oncology*. <https://doi.org/10.1007/978-3-319-19563-6>
15. Carrascosa PM, Cury RC, Garcia MJ, Leipsic JA (2015) Dual-Energy CT. *Cardiovasc Imaging*. <https://doi.org/10.1007/978-3-319-21227-2>
16. Dobeil KL, Lewis SJ, Meikle SR, Thiele DL, Brennan PC (2013) Noise-reducing algorithms do not necessarily provide superior dose optimisation for hepatic lesion detection with multidetector CT. *Br J Radiol*. <https://doi.org/10.1259/bjr.20120500>
17. Aurumskjold ML, Ydstro K, Tingberg A, Söderberg M (2016) Improvements to image quality using hybrid and model-based iterative reconstructions: a phantom study. *Acta Radiol*. <https://doi.org/10.1177/0284185116631180>
18. Kligerman S, Mehta D, Farnadash M, et al. (2013) Use of a hybrid iterative reconstruction technique to reduce image noise and improve image quality in obese patients undergoing computed tomographic pulmonary angiography. *J Thorac Imaging* 28:49–59. <https://doi.org/10.1097/RTI.0b013e31825412b2>
19. Shuman WP, Chan KT, Busey JM, et al. (2014) Standard and reduced radiation dose liver CT images: adaptive statistical iterative reconstruction vs. model-based iterative reconstruction—comparison of findings and image quality. *Radiology* 273:793–800. <https://doi.org/10.1148/radiol.14140676>
20. Vonder M, Pelgrim GJ, Meyer M, et al. (2017) Dose reduction techniques in coronary calcium scoring: the effect of iterative reconstruction combined with low tube voltage on calcium scores in a thoracic phantom. *Eur J Radiol* 93:229–235. <https://doi.org/10.1016/j.ejrad.2017.06.001>
21. Schneider D, Apfaltrer P, Sudarski S, et al. (2014) Optimization of kiloelectron volt settings in cerebral and cervical dual-energy CT angiography determined with virtual monoenergetic imaging. *Acad Radiol* 21:431–436. <https://doi.org/10.1016/j.acra.2013.12.006>
22. Albrecht MH, Scholtz J-E, Hüsters K, et al. (2016) Advanced image-based virtual monoenergetic dual-energy CT angiography of the abdomen: optimization of kiloelectron volt settings to improve image contrast. *Eur Radiol* 26:1863–1870. <https://doi.org/10.1007/s00330-015-3970-2>
23. Apfaltrer P, Sudarski S, Schneider D, et al. (2014) Value of monoenergetic low-kV dual energy CT datasets for improved image quality of CT pulmonary angiography. *Eur J Radiol* 83:322–328. <https://doi.org/10.1016/j.ejrad.2013.11.005>
24. Sudarski S, Apfaltrer P, Nance JW, et al. (2014) Objective and subjective image quality of liver parenchyma and hepatic metastases with virtual monoenergetic dual-source dual-energy CT reconstructions. An analysis in patients with gastrointestinal stromal tumor. *Acad Radiol* 21:514–522. <https://doi.org/10.1016/j.acra.2014.01.001>
25. Aurumskjöld M-L, Ydstrom K, Tingberg A, Söderberg M (2017) Improvements to image quality using hybrid and model-based iterative reconstructions: a phantom study. *Acta Radiol* 58:53–61. <https://doi.org/10.1177/0284185116631180>
26. Khawaja RDA, Singh S, Otrakji A, et al. (2015) Dose reduction in pediatric abdominal CT: use of iterative reconstruction techniques across different CT platforms. *Pediatr Radiol* 45:1046–1055. <https://doi.org/10.1007/s00247-014-3235-2>
27. Altenbernd J, Heusner TA, Ringelstein A, et al. (2011) Dual-energy-CT of hypervascular liver lesions in patients with HCC: investigation of image quality and sensitivity. *Eur Radiol* 21:738–743. <https://doi.org/10.1007/s00330-010-1964-7>
28. Grant KL, Flohr TG, Krauss B, et al. (2014) Assessment of an Advanced image-based technique to calculate virtual monoenergetic computed tomographic images from a dual-energy examination to improve contrast-to-noise ratio in examinations using iodinated contrast media. *Invest Radiol* 49:586–592. <https://doi.org/10.1097/RLI.0000000000000060>
29. Leng S, Yu L, Fletcher JG, McCollough CH (2015) Maximizing iodine contrast-to-noise ratios in abdominal CT imaging through use of energy domain noise reduction and virtual monoenergetic dual-energy CT. *Radiology* 276:562–570. <https://doi.org/10.1148/radiol.2015140857>
30. Kalender WA, Klotz E, Kostaridou L (1988) An algorithm for noise suppression in dual energy CT material density images. *IEEE Trans Med Imaging* 7:218–224. <https://doi.org/10.1109/42.7785>
31. Kelcz F, Joseph PM, Hilal SK (1979) Noise considerations in dual energy CT scanning. *Med Phys* 6:418–425. <https://doi.org/10.1118/1.594520>
32. Chang W, Lee JM, Lee K, et al. (2013) Assessment of a model-based, iterative reconstruction algorithm (MBIR) regarding image quality and dose reduction in liver computed tomography. *Invest Radiol* 48:598–606. <https://doi.org/10.1097/RLI.0b013e3182899104>
33. Husarik DB, Gordic S, Desbiolles L, et al. (2015) Advanced virtual monoenergetic computed tomography of hyperattenuating and hypoattenuating liver lesions. *Invest Radiol* 50:695–702. <https://doi.org/10.1097/RLI.0000000000000171>
34. Willemink MJ, Leiner T, De Jong PA, et al. (2013) Iterative reconstruction techniques for computed tomography part 2: initial results in dose reduction and image quality. *Eur Radiol* 23:1632–1642. <https://doi.org/10.1007/s00330-012-2764-z>
35. Ruoqiao Zhang R, Thibault J-B, Bouman CA, Sauer KD, Jiang Hsieh J (2014) Model-based iterative reconstruction for dual-energy X-ray CT using a joint quadratic likelihood model. *IEEE Trans Med Imaging* 33:117–134. <https://doi.org/10.1109/TMI.2013.2282370>